Instrument Science Report COS 2018-20(v1)

Flat Fields and Flux Calibrations for the COS FUV Channel at Lifetime Position 4

William J. Fischer[1], Marc Rafelski[1], and Gisella de Rosa[1]

[1] Space Telescope Science Institute, Baltimore, MD

25 September 2018

ABSTRACT

As part of the calibration of the fourth lifetime position (LP4) of the Cosmic Origins Spectrograph (COS) Far-Ultraviolet (FUV) detector, we derived low-order flat fields (L flats) and sensitivities. To do this, spectra of the star WD 0308–565 were obtained with the G130M, G160M, and G140L gratings, and spectra of the star GD 71 were obtained with the G160M grating, all through the Primary Science Aperture (PSA). Observations were executed with all cenwaves and all FP-POS with the exception of G130M/1055 and G130M/1096, which remained at LP2. The L flats and sensitivities at LP4 were derived with the same method as at LP3. The L flats at LP4 agree with those at LP3 to within $\sim$ 2%, depending on grating and detector position. The sensitivities at LP4 are as expected after accounting for the previously characterized time-dependent sensitivity of the FUV detector. The relative and absolute flux calibration accuracies at LP4 are within the specifications of 2% and 5%.

Contents

1. Introduction

The COS FUV detector is susceptible to gain sag, a reduction in the ability of the detector to convert incoming photons to electrons that becomes more severe with continued use. To counteract this effect, the location where FUV spectra fall on the detector (the lifetime position or LP) is periodically moved to an unused and therefore pristine region. On July 23, 2012, spectra were moved to LP2, offset by $+3.5''$ from LP1 in the cross-dispersion direction. On February 9, 2015, spectra were moved to LP3, offset by $-2.5''$ from LP1. Operations of the COS FUV detector at LP4, located at $-5.0''$ from LP1, started on October 2, 2017 for all cenwaves except 1055 and 1096 of the G130M grating, which remained at LP2.

At each new lifetime position, the resolution changes, worsening with increased angular separation from LP1 (Fox et al. 2018, ISR 2018-07), the flat field may change due to the new location of spectra on the detector, and the throughputs are remeasured to verify their consistency with the established requirements. To maintain the targeted absolute and relative flux calibration accuracies for COS ($< 5\%$ and $< 2\%$, respectively) and meet other specifications, each change in lifetime position requires a new calibration effort. In this ISR, which is part of a series describing the LP4 calibration program, we report on the generation of new flat fields and sensitivity curves for LP4.

The COS flat field is conventionally separated into an L flat, which contains variations in the detector response that have low spatial frequency, and a P flat, which accounts for pixel-to-pixel variations. The L flats are available as reference files and are incorporated in the standard COS calibration routine. The P flats are not applied in routine calibration. Instead, the influence of pixel-to-pixel variations can be reduced with the standard COS observing strategy, where spectra are obtained at multiple positions (FP-POS) spaced along the dispersion direction of the detector and then co-added. The maximum signal-to-noise ratio attainable with this strategy depends on the grating and segment and varies from $\sim$ 30 to 50 (Table 5.6 of the COS Instrument Handbook). If higher signal-to-noise ratios are desired, P flats may be useful; they are available upon request from the STScI help desk.

At LP1 and LP2, L flats were constructed by iteratively decomposing net-count spectra into a position-dependent flat field and a wavelength-dependent spectrum. The flat field was interactively fit with a low-order polynomial or spline function, and sensitivity curves were then calculated from spectra that had been flat-fielded with the final

Table 1. Spectra Used for Flat Creation and Flux Calibration – Program 14910

Star	Grating	Cenwaves	Segment
WD 0308–565	G130M	1222, 1291, 1300, 1309, 1318, 1327	BOTH
WD 0308–565	G160M	1577, 1589, 1600, 1611, 1623	BOTH
WD 0308–565	G140L	1105	FUVA
WD 0308–565	G140L	1280	BOTH
GD 71	G160M	1577, 1589, 1600, 1611, 1623	FUVA

L flats (Massa et al. 2014, ISR 2013-09). This approach required input from the user in the form of manual selection of nodes for the fitting and manual creation of a function to fit the 1180 Å feature (Section 3.1). A different procedure was used at LP3 (Debes et al. 2016, ISR 2016-15). In the revised procedure, there is limited input from the user, with a fixed number of equally separated nodes for each spectrum, although the assumptions are retained that, for a given detector setting, the flat field depends only on position and the sensitivity curve depends only on wavelength. Debes et al. showed that their more easily reproducible approach gave similar results to the original one. At LP4 we continue to use the procedure developed for LP3.

In this report we describe the construction of L flats and sensitivity curves for LP4 based on data that were obtained there in April 2017, before the move to LP4 for general observing programs. In Section 2 we list the calibration observations used in the program, and in Section 3 we review the methodology for constructing the flats and sensitivity curves and plot them. In Section 4 we compare the results to those obtained at LP3, in Section 5 we discuss the scientific validation of the files, and in Section 6 we give our conclusions.

2. Observations

The spectra used to derive the flats and sensitivities were obtained through the Primary Science Aperture (PSA) at LP4 in program 14910, "Fourth COS FUV Lifetime Position: Cross-Dispersion Profiles, Flux, and Flat-Field Calibration" (PI M. Rafelski), which was executed in April 2017. Table 1 lists the observed cenwaves. The only cenwaves that were not observed are those that remained at LP2 (G130M/1055 and 1096). Spectra of the hot subdwarf WD 0308–565 were obtained with all modes, and, due to the diminishing flux of that target at long wavelengths, spectra of the white dwarf GD 71 were obtained for segment A of all G160M cenwaves. All modes were observed at all four FP-POS.

3. Generation of L Flats and Sensitivity Curves

Our approach assumes that the flat fields reflect the detector response and are thus a function of the detector coordinates only, while the sensitivity curves describe the remaining throughput of the telescope plus instrument and are thus a function only of wavelength. Flats are generated for each grating and segment, while sensitivity curves are generated for each grating, segment, and cenwave.

We used the IDL procedure `derive_cos_flats.pro` (G. Becker) to generate the flat fields and sensitivity curves with the method outlined in Debes et al. (2016). The net counts are assumed to be the product of the flux from the source, the flat field, and the sensitivity, or

$$N(x, \lambda) = S(\lambda)F(x)R(\lambda),$$

where $N(x, \lambda)$ are the net counts at detector position x and wavelength λ, $S(\lambda)$ is the flux, $F(x)$ is the flat field, and $R(\lambda)$ is the response (sensitivity) function. We observed HST standards, where S_λ is well known, and we used multiple cenwave and FP-POS settings to sample each position on the detector at multiple wavelengths. This breaks the degeneracy between x and λ, allowing the flat and the sensitivity to be constrained independently.

To fit the L flats, we used a cubic spline with 20 nodes spaced evenly over the range in x covered by well calibrated data. For the sensitivity curves, we used piecewise quadratic interpolation. Generally there were 15 nodes over the range in λ covered by all four FP-POS, except for G140L, where 30 points were used, and for segment B of G130M, where 20 points were used to give flexibility in fitting the 1180 Å feature (Section 3.1).

The fitting is performed on net counts spectra that were calibrated using a flat field that contains only grid wire shadows and "impostors." The shadows are due to grid wires, 17 on segment A and 22 on segment B, that improve the quantum efficiency of the detector and induce a drop in response of about 20% over a width of about 50 pixels (Ely et al. 2011, ISR 2011-03). The impostor grid wire shadows appear only on segment B and are an artifact introduced by the geometric distortion correction (Section 5.8.1 of the COS Instrument Handbook).

Each FUV grating (G130M, G160M, G140L) and segment (A or B) has its own flat field of 16384 columns by 1024 rows. (Relatively little data are obtained on segment B with G140L, so this flat is a copy of the one for G130M/B.) The L flats derived here depend on column (the dispersion direction), and each is replicated over 1024 rows (the cross-dispersion direction). Grid-wire shadows and impostor shadows, which are the only features included in the flats that vary with row, are then added back into the flats.

The sensitivity curves are provided in a FITS table with one entry for each combination of cenwave, segment, and aperture. They are corrected for the time-dependent sensitivity (TDS) of each grating as measured in FUV TDS calibration programs (De Rosa 2018, ISR 2018-09). Figures 1 and 2 show the one-dimensional flats and sensitivity curves derived with these procedures. Sensitivities for the Bright Object Aperture

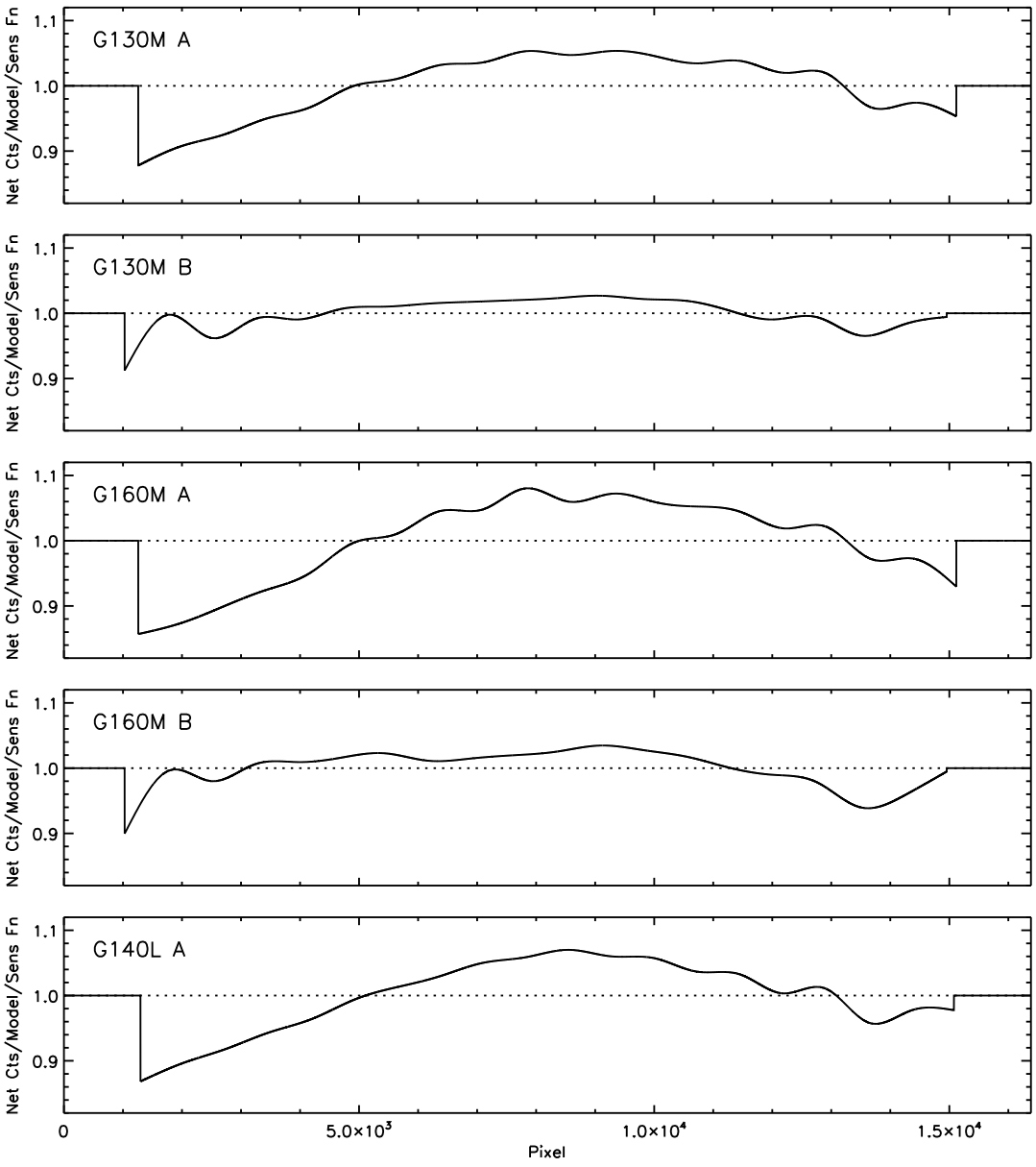

Figure 1. L flats for LP4. In the delivered reference files, the L flats shown here, which depend only on detector column, are replicated for each row of the detector. The signatures of the gridwire shadows and impostors are then included. Because only the extreme red end of G140L/B is well calibrated, the flat for G130M/B is used for that segment.

(BOA), not shown, were obtained by multiplying those derived for the PSA by the wavelength-dependent transmission curve of the BOA (Figure 8 of Massa et al. 2010, ISR 2010-02).

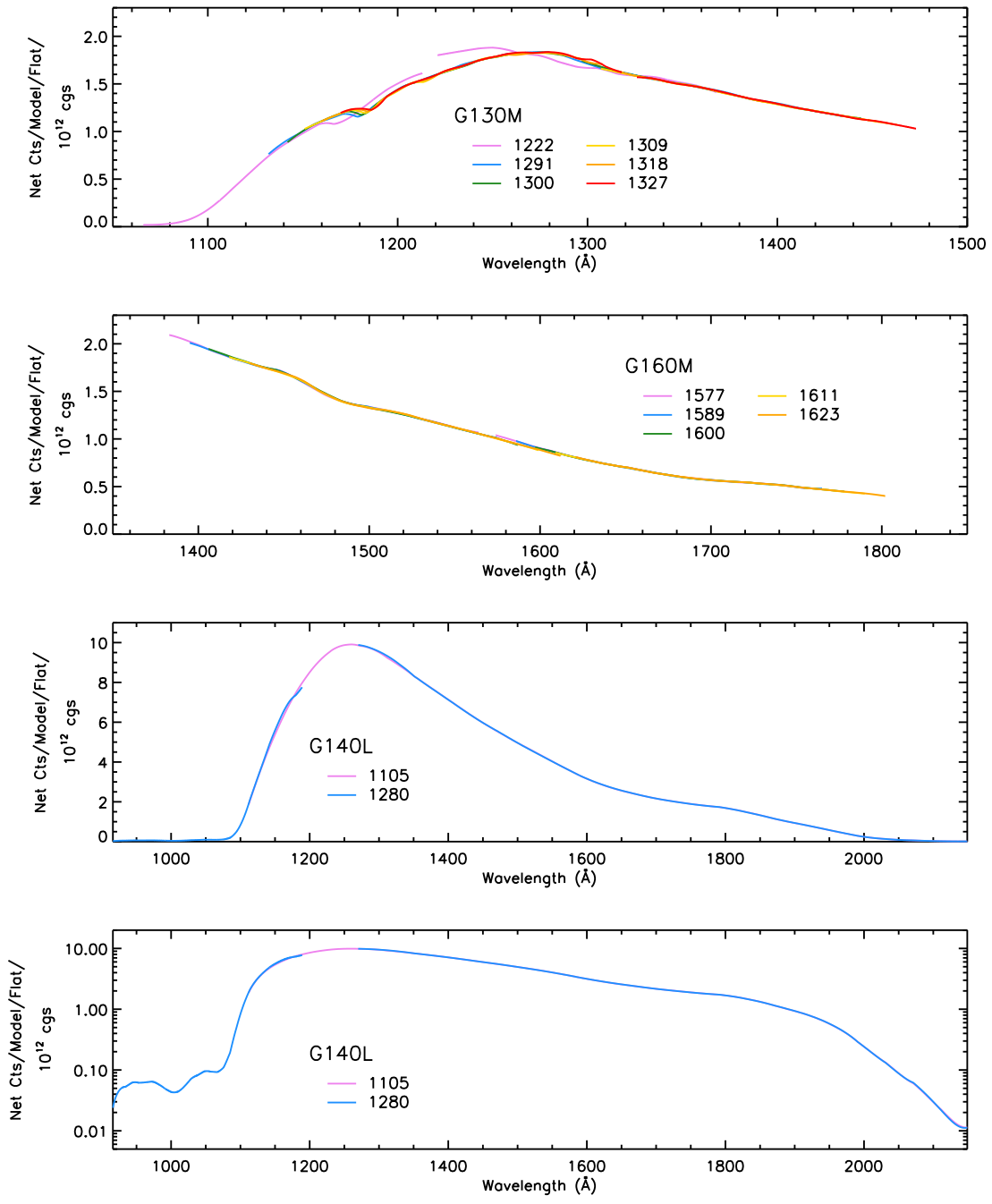

Figure 2. Sensitivity curves at LP4 for each cenwave. Curves for segments A and B are shown in the same panel. The curves for G140L are also shown with a logarithmic vertical axis to highlight their behavior at short wavelengths.

3.1 Removal of the 1180 Å Feature

Wood's anomalies (Wood 1902; Maystre 2012) appear near wavelengths

$$\lambda = d(\sin\alpha \pm 1)/n,$$

where d is the groove separation of the grating, n is a non-zero integer, and α is the incidence angle. This is the wavelength for which a scattered wave propagates tangentially to the grating surface. For the COS G130M grating, $\lambda \sim d$, and it is therefore subject to such an anomaly, which manifests as a dip in sensitivity on Segment B, near 1180 Å. Since the wavelength of a Wood's anomaly depends on the incidence angle, the wavelength of the dip varies mildly with cenwave as the optics select mechanism (OSM1) is rotated to different positions.

Figure 3 shows how we fit and remove the 1180 Å feature by including extra nodes in the fitting function. The fitting function then automatically traces the feature, and it is removed when we divide by the fit. No assumptions are made about the central wavelength, depth, or shape of the sensitivity depression.

4. Comparison of LP4 Flats and Sensitivities to Those at LP3

In Figure 4 we compare the L flats derived for LP3 by Debes et al. (2016) to those we derived for LP4. The L flats differ by up to 2% over most of each segment, with variations of up to 8% at the edges of segment A. These are likely due to subtle differences in the response of the detector at $-2.5''$ from LP3.

The COS FUV gratings and detector segments decline in sensitivity with time. This time-dependent sensitivity (TDS) is characterized and reported elsewhere (e.g., De Rosa 2017, ISR 2017-10). A direct comparison of sensitivities between LP3 and LP4 is not possible due to the difficulty in disentangling the TDS from other effects, but there is no indication of a significant change in sensitivity at LP4 beyond that expected from TDS.

5. Scientific Validation of Flats and Sensitivities

In this section we demonstrate that the L flats and sensitivity curves can be applied to spectra of the net counts to yield accurately flux-calibrated spectra. In Figures 5 and 6, we show the effect of the flat correction. Uncorrected counts, in the left column of the figure, disagree at a given wavelength when sampled at different positions on the detector with different cenwaves. After the flat fields are applied, on the right column of the figure, each cenwave gives the same number of counts at each wavelength. This shows that the spectra have been corrected for elements of the detector response that vary slowly with position.

The flat correction leaves cenwave 1222 mildly out of agreement with the other G130M cenwaves on segment A; the effect is more significant on segment B. This was

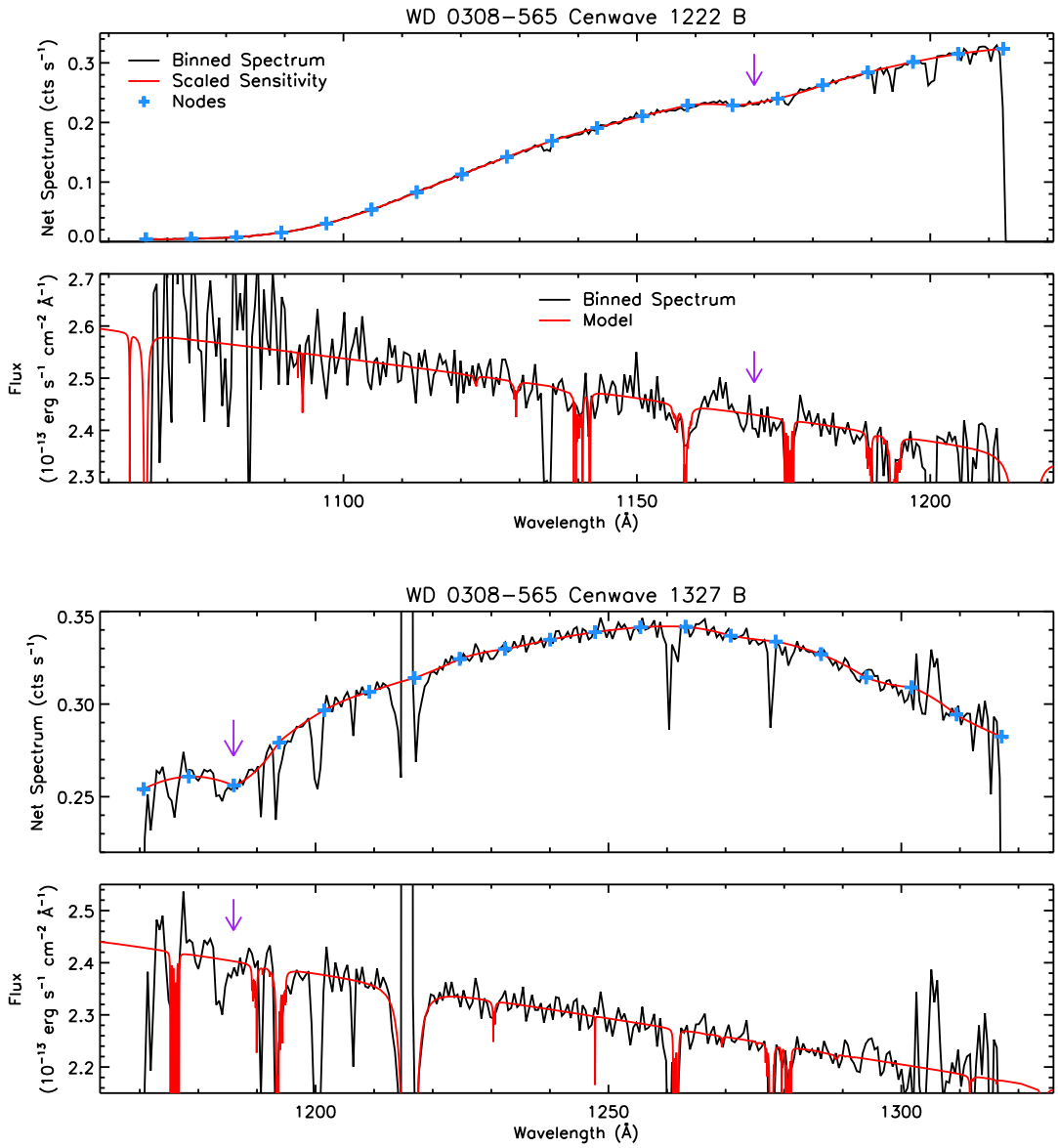

Figure 3. Removal of the 1180 Å feature from G130M/B spectra. Purple arrows point to the affected wavelengths. The extreme cenwaves are plotted to show how the wavelength of the feature increases slightly with increasing cenwave, from 1170 Å for cenwave 1222 to 1186 Å for cenwave 1327. The top plot of each pair shows the net counts, the spline nodes, and the sensitivity function. (For clarity, the sensitivity function is scaled to align with the spectrum.) The bottom plot of each pair shows how spectra calibrated with a sensitivity function that includes the 1180 Å feature align well with the model, including in the region around the feature.

also the case at LP3. We have assumed that the conversion from counts to flux takes place in two steps: a flat correction that depends only on grating, not cenwave, and a

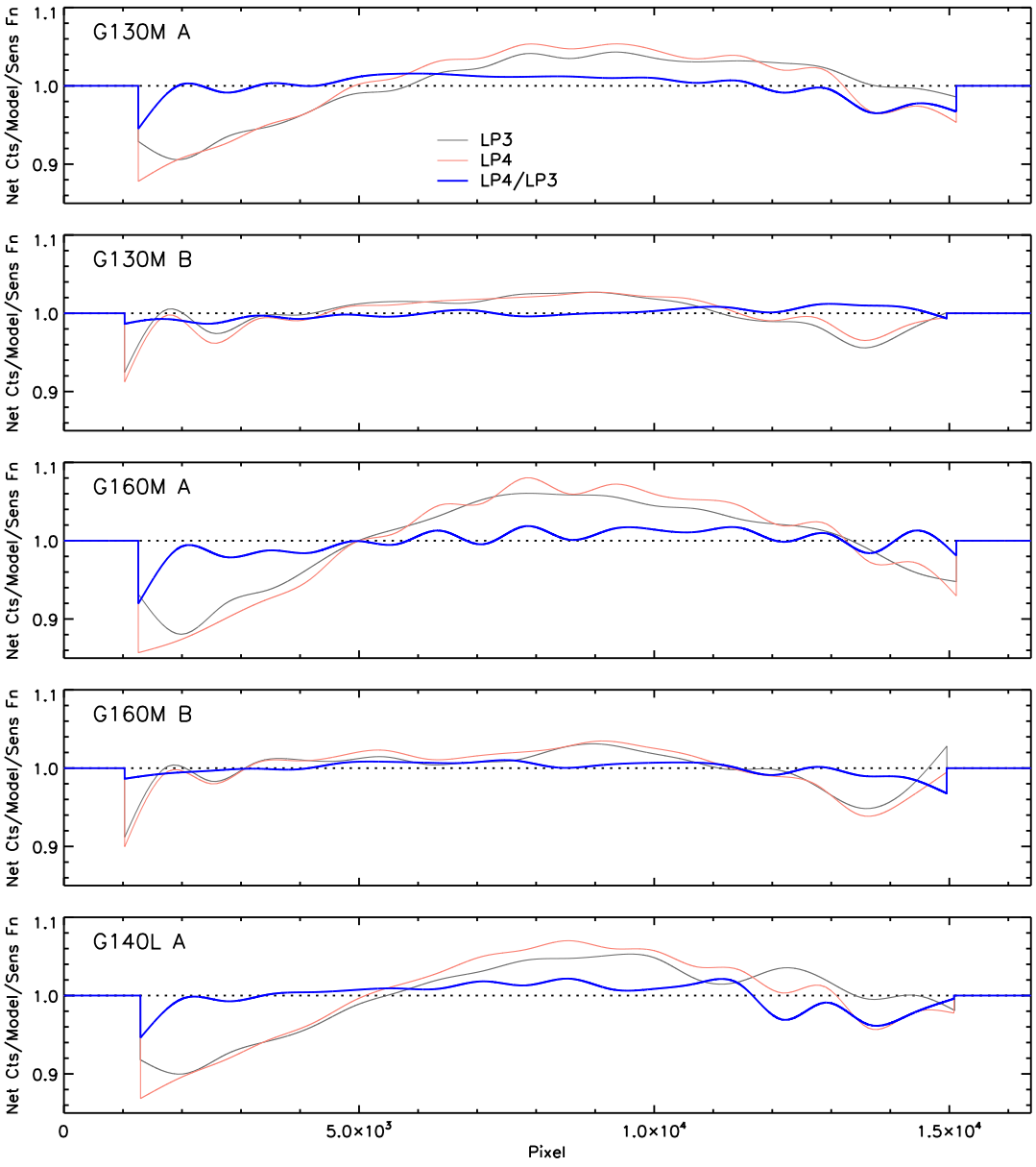

Figure 4. Comparison of L flats at LP3 and LP4 (gray and salmon curves). The blue curves show their ratios. (The units on the vertical axis apply to the flats; their ratios are dimensionless.) Except at the edges of the segments, the L flats from LP3 and LP4 generally agree to within 2%.

flux correction that depends on the cenwave. For the extreme OSM1 rotation of cenwave 1222, the assumption that the flat field is independent of cenwave appears to be mildly violated. The residual disagreement of 1222 with other cenwaves is removed in the flux calibration, as demonstrated in the following paragraphs.

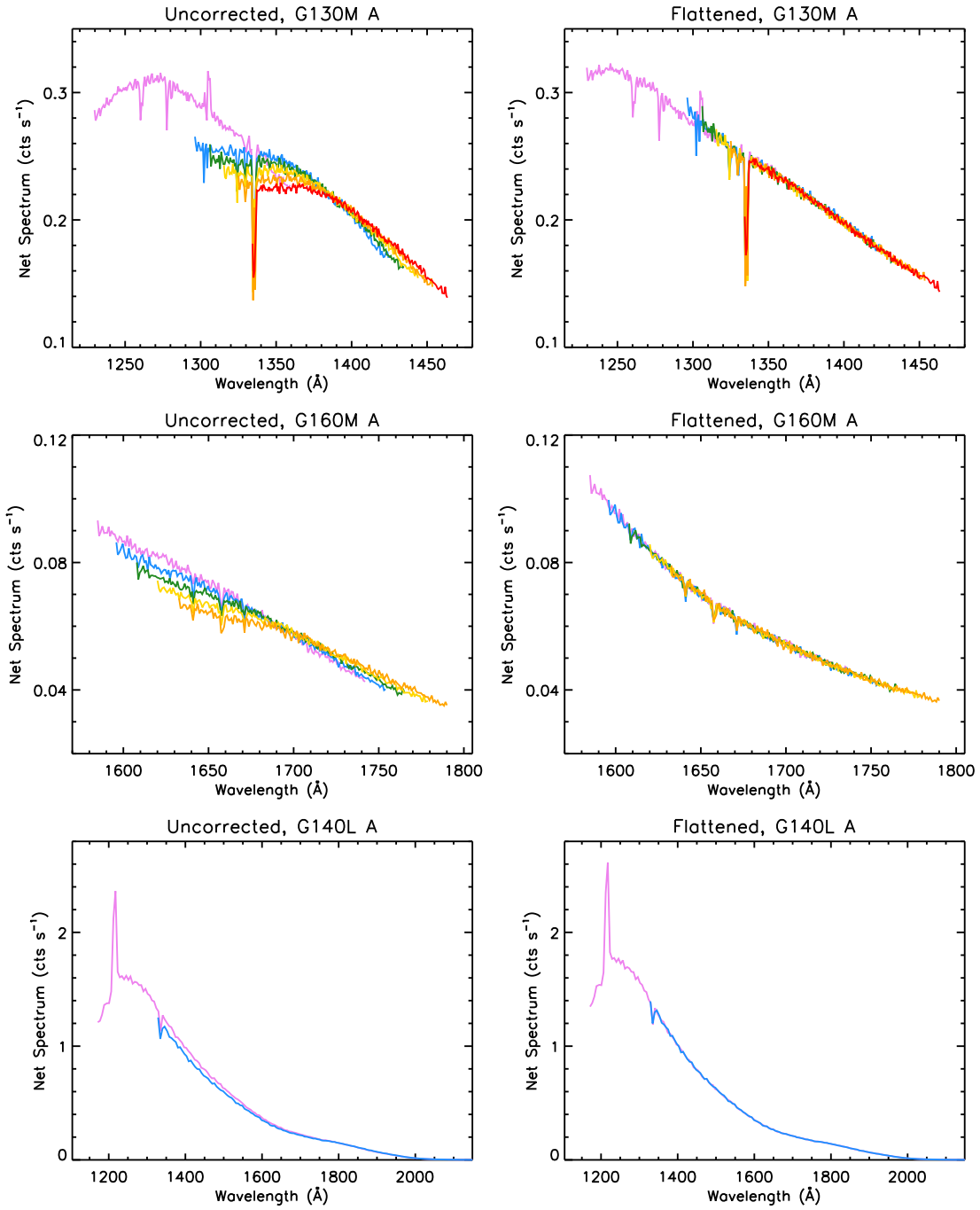

Figure 5. Spectra of WD 0308–565 that demonstrate the effectiveness of the flat correction for segment A. Cenwaves are color-coded the same way as in Figure 2. The flat correction is successful because, after it is applied (right column), spectra from different cenwaves agree at each wavelength. Emission features at 1302 Å (top row) and 1216 Å (bottom row) are due to O I and Ly α airglow, respectively. For G130M, cenwave 1222 (pink) is not completely brought into agreement with the others. This is rectified in the flux calibration step; see the text for discussion.

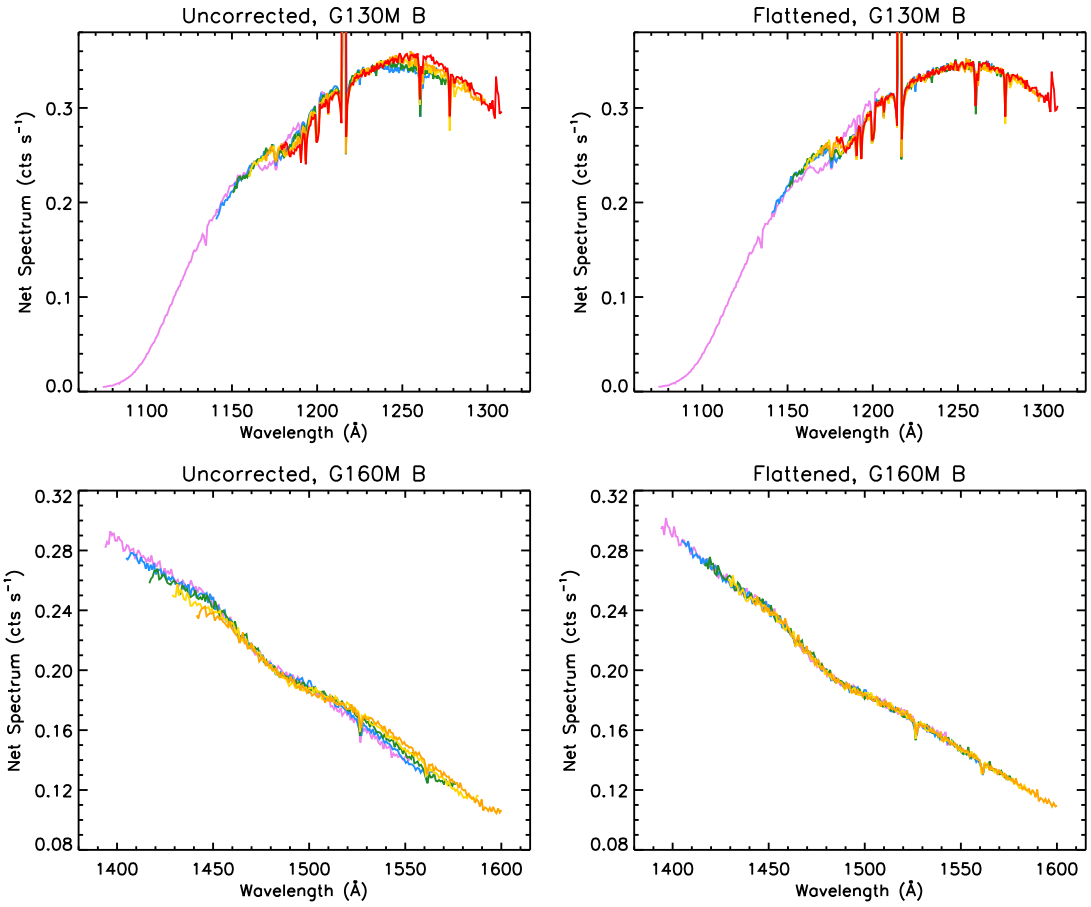

Figure 6. Spectra of WD 0308–565 that demonstrate the effectiveness of the flat correction for segment B. Cenwaves are color-coded the same way as in Figure 2. The flat correction is successful because, after it is applied (right column), spectra from different cenwaves agree at each wavelength. Emission features at 1216 Å and 1302 Å (top row) are due to Ly α and O I airglow, respectively. For G130M, cenwave 1222 (pink) is not completely brought into agreement with the others, and the 1180 Å feature persists. These issues are rectified in the flux calibration step; see the text for discussion. G140L has just one cenwave that uses segment B, so no comparison is possible.

In Figures 7, 8, and 9, we show the effect of the flux calibration. Spectra calibrated with the L flats and sensitivities derived for LP4 are binned by 0.6 Å for the M modes and 4.8 Å for the L modes. The spectra agree with the models in that the residuals average to about zero and have little bin-to-bin scatter. Over all modes, the mean difference between the calibrated observed flux and model flux is at most 0.5%.

The standard deviations in the observed-to-model flux ratios are small. For the M modes other than 1222/B, they are less than 1.5%. At the blue end of 1222/B, the spread is larger; it is 1.1% at wavelengths greater than 1100 Å but climbs to 2.9% at shorter wavelengths. For the L modes, the standard deviations of the residuals are less

than 1.8% between 1100 and 2000 Å, and they rise to 5–8% above and below this range, where the absolute sensitivities are low.

6. Conclusions

The method developed to derive flats and sensitivities at LP3 continues to work well at LP4. We applied this method to spectra of WD 0308–565 and GD 71 obtained in April 2017 at LP4. The resulting L flats differ from those derived for LP3 by $\sim 2\%$ depending on detector position and grating, and the sensitivities are as expected after accounting for time dependence. The resulting flat fields bring adjacent cenwaves into excellent agreement, and the sensitivity curves generate spectra that agree with models to within the specifications of 2% relative and 5% absolute.

Change History for COS ISR 2018-20

Version 1: 25 September 2018- Original Document

References

Debes, J. H., Becker, G., Roman-Duval, J., et al. 2016, Instrument Science Report COS 2016-15, "Third COS FUV Lifetime Calibration Program: Flatfield and Flux Calibrations"

De Rosa, G. 2018, Instrument Science Report COS 2018-09, "Cycle 24 COS/FUV Spectroscopic Sensitivity Monitor"

Ely, J., Massa, D., Ake, T., et al. 2011, Instrument Science Report COS 2011-03, "COS FUV Gridwire Flat Field Template"

Fox, A., James, B., Roman-Duval, J., Rafelski, M., & Sonnentrucker, P. 2018, Instrument Science Report COS 2018-07, "The Spectral Resolution of the COS FUV Channel at Lifetime Position 4"

Massa, D., Ely, J., Osten, R., et al. 2014, Instrument Science Report COS 2013-09, "Updated Absolute Flux Calibration of the COS FUV Modes"

Massa, D., Keyes, C., Penton, S., Bolin, R., & Froning, C. 2010, Instrument Science Report COS 2010-02, "SMOV Absolute Flux Calibration of the COS FUV Modes"

Maystre, D. 2012, in Springer Ser. in Optical Sciences 167, Plasmonics, ed. S. Enoch & N. Bonod (Berlin: Springer-Verlag), 39

Wood, R. W. 1902, Philos. Mag. 4, 396

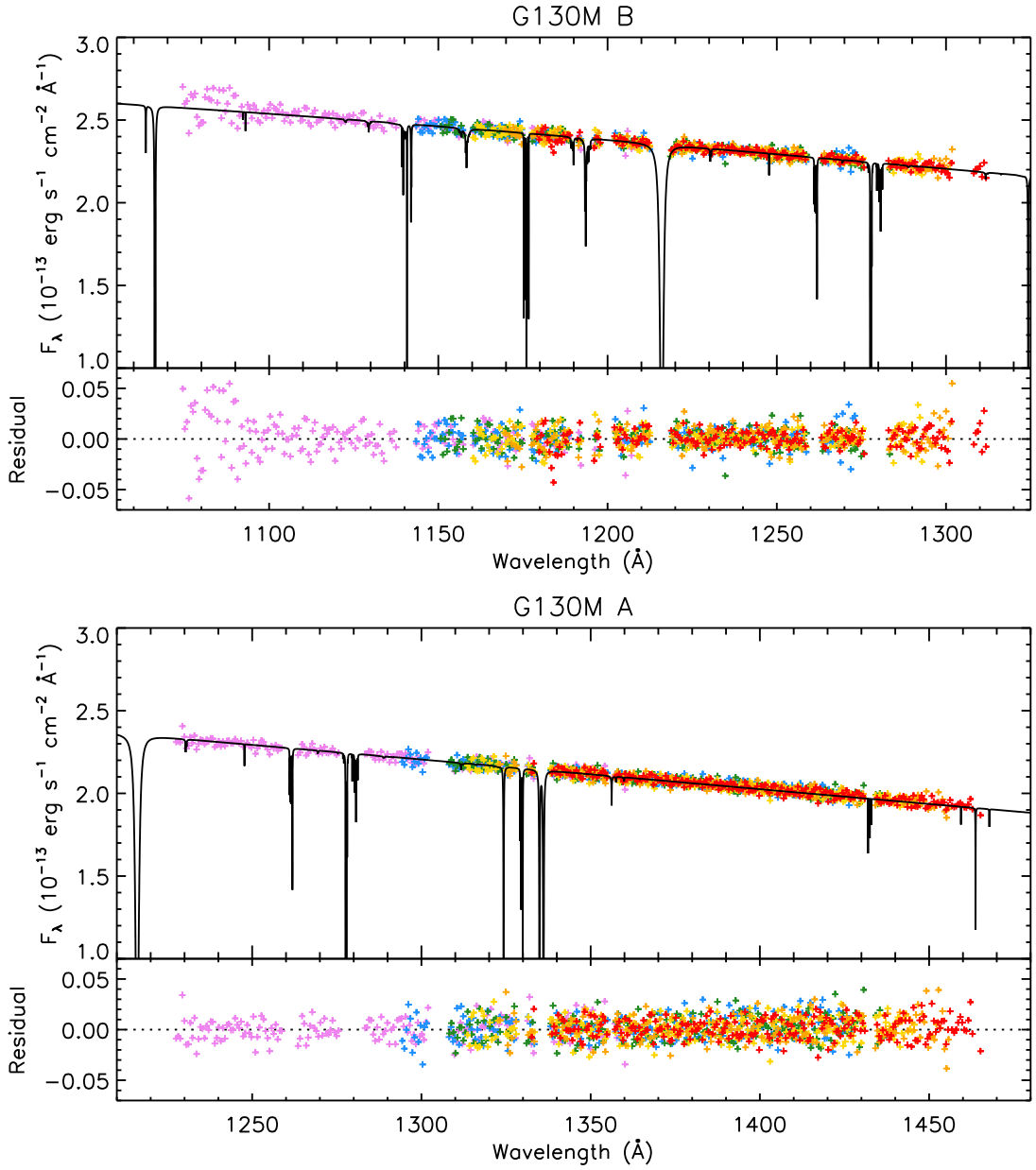

Figure 7. A demonstration of the accuracy and precision of the flux calibration for both segments with the G130M grating. Colored symbols are the COS data for WD 0308–565, binned by 0.6 Å. Colors map to cenwaves as in previous figures. The black curves are the model spectra. Absorption and airglow lines and the detector edges are excluded from the analysis. The overall agreement between the colored symbols and the black curves ($< 0.5\%$ mean difference) demonstrates good absolute flux calibration, while the small scatter in the colored symbols (standard deviations $< 1.5\%$ above 1100 Å) demonstrates good relative flux calibration.

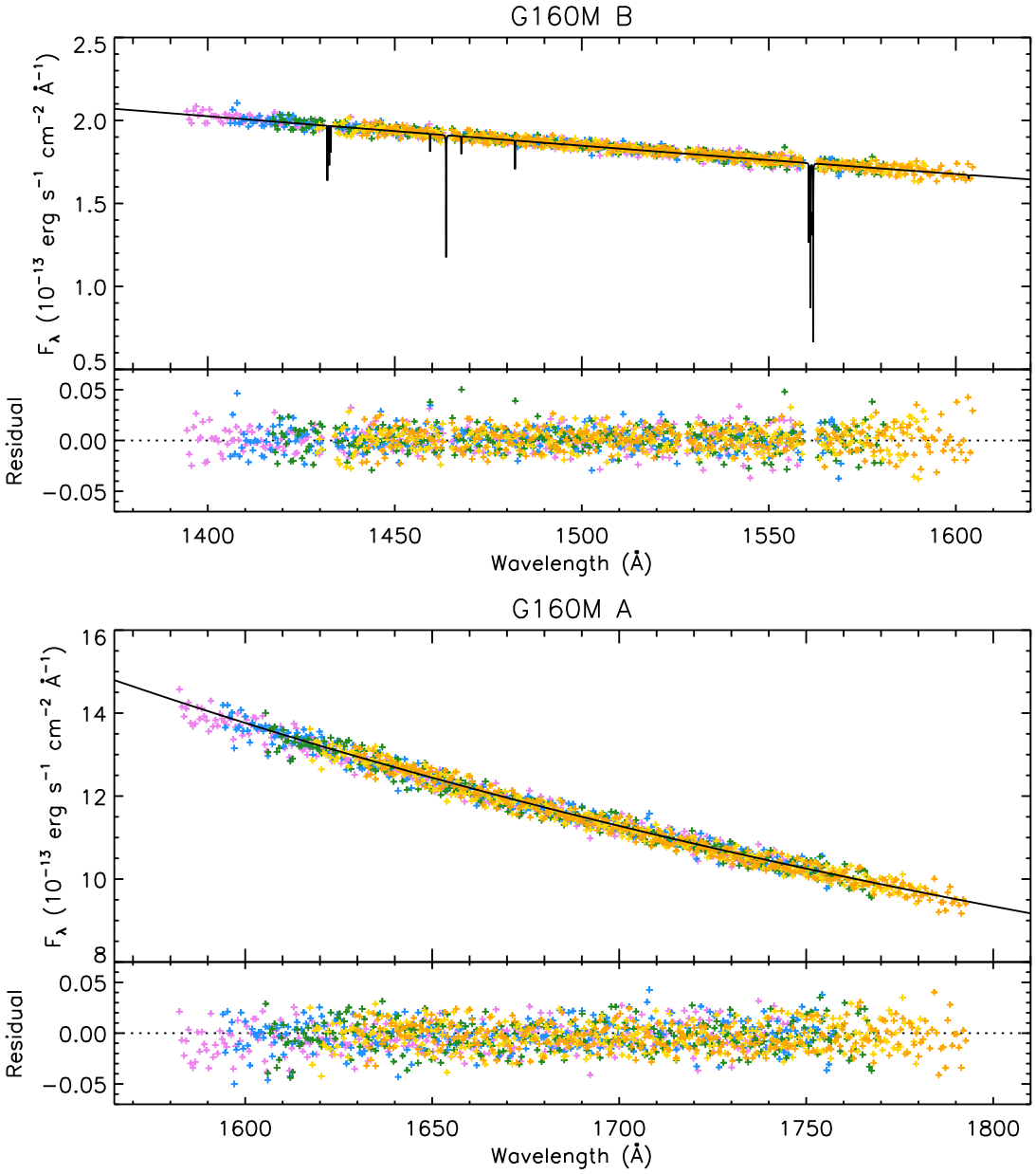

Figure 8. A demonstration of the accuracy and precision of the flux calibration for both segments with the G160M grating. Colored symbols are the COS data, binned by 0.6 Å. Colors map to cenwaves as in previous figures. The black curves are the model spectra. We used GD 71 for segment A and WD 0308–565 for segment B. Absorption and airglow lines and the detector edges are excluded from the analysis. The overall agreement between the colored symbols and the black curves ($< 0.5\%$ mean difference) demonstrates good absolute flux calibration, while the small scatter in the colored symbols (standard deviations $< 1.5\%$) demonstrates good relative flux calibration.

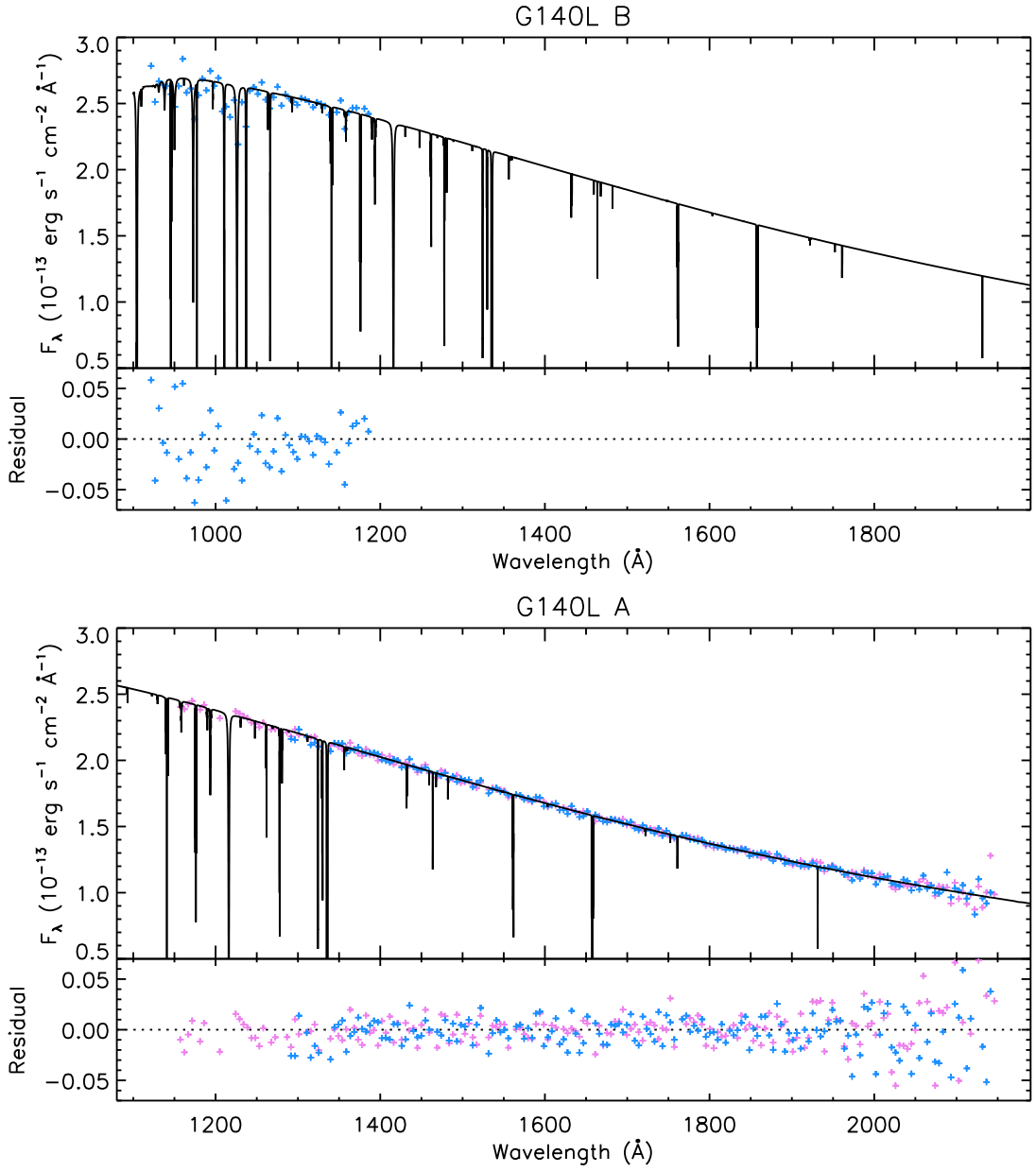

Figure 9. A demonstration of the accuracy and precision of the flux calibration for both segments with the G140L grating. Colored symbols are the COS data for WD 0308–565, binned by 4.8 Å. Colors map to cenwaves as in previous figures. The black curves are the model spectra. Absorption and airglow lines and the detector edges are excluded from the analysis. The overall agreement between the colored symbols and the black curves ($< 0.5\%$ mean difference) demonstrates good absolute flux calibration, while the small scatter in the colored symbols (standard deviations $< 1.8\%$ between 1100 and 2000 Å) demonstrates good relative flux calibration.